Finite element analyses of rail head cracks: Predicting direction and rate of rolling contact fatigue crack growth
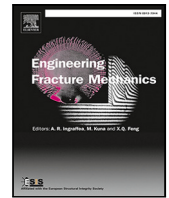
N.B. When citing this work, cite the original published paper.

(article starts on next page)

Finite element analyses of rail head cracks: Predicting direction and rate of rolling contact fatigue crack growth

Mohammad Salahi Nezhad [a],*, Fredrik Larsson [a], Elena Kabo [b], Anders Ekberg [b]

[a] Department of Industrial and Materials Science/CHARMEC, Chalmers University of Technology, SE-412 96 Gothenburg, Sweden
[b] Department of Mechanics and Maritime Sciences/CHARMEC, Chalmers University of Technology, SE-412 96 Gothenburg, Sweden

ARTICLE INFO

ABSTRACT

A numerical framework in 3D for predicting crack growth direction and rate in a rail head is presented. An inclined semi-circular surface-breaking gauge corner crack with frictionless crack faces is incorporated into a 60E1 rail model. The investigated load scenarios are wheel–rail contact, rail bending, thermal loading, and combinations of these. The crack growth direction is predicted using an accumulative vector crack tip displacement criterion, and Paris-type equations are employed to estimate crack growth rates. Results are evaluated along the crack front for varying crack radii and crack plane inclinations. Under the combined load cases and in the presence of tractive forces, the crack is generally predicted to go deeper into the rail than under pure contact. Crack growth rates for the combined load cases are higher than (but still close to) that for pure contact. A tractive force will increase growth rates for smaller cracks, whereas a steeper (45°) inclination will decrease the growth rate under the studied conditions as compared to a shallower (25°) inclination. Results should be of use for rail maintenance planning where deeper cracks require more machining efforts.

1. Introduction

Railway transportation is safe, efficient, generally reliable, and has a low carbon footprint [1]. One of the major challenges in ensuring safety and punctuality is managing Rolling Contact Fatigue (RCF) cracks. These cracks can be costly to mitigate and/or result in safety risks if not treated in time [2]. In general, an RCF crack that grows shallowly into a rail may cause material spalling/fall-out and requires maintenance. However, it does not impose an imminent risk of rail break, which is the case for a transversely deviating crack. Having reliable simulation models that can predict under which circumstances transverse growth is likely is thus crucial for maintenance planning.

The numerical models need to account for rolling contact with large compressive and shear stresses at the wheel–rail interface. Further, thermal loading due to restricted contraction, and rail bending need to be considered. As a consequence, crack growth under complex general non-proportional mixed-mode loading needs to be assessed. The majority of criteria in the literature fail to account for such loading. Moreover, a 3D model is required as the wheel–rail contact load is a 3D load that is not possible to consistently scale to 2D conditions. Another complicating factor for the numerical investigations of RCF cracks is that there is a lack of controlled experimental data, which makes the model validation difficult.

Head checks and squats are two of the most common types of RCF cracks in railways [3]. Head checks appear at the gauge corner in curves as an array of inclined, tightly spaced surface cracks. They are initiated due to plastic strain accumulation mainly caused by frictional wheel–rail contact [4]. Squats are seen on the running band of (near) tangent tracks as isolated depressions.

They are initiated mainly by rail surface defects, e.g., indentations, martensite, and short-pitch corrugations, and the high-frequency dynamic forces resulting from these [4].

The majority of the numerical studies available in the literature are focused on the variations of the Stress Intensity Factor (SIF) over a load cycle. A semi-analytical method is employed in [5] to investigate the influence of crack face friction, hydrostatic lubrication, and fluid entrapment on SIF histories during a wheel passage for a surface-initiated RCF crack in a 2D model. Bogdanski and co-workers performed extensive studies on the influential parameters on the evolution of SIF over a wheel passage for 'squat'-type RCF cracks in 2D and 3D, studying among other things the influence of crack (plane) inclination [6], residual stresses [6,7], crack face friction [7], and fluid entrapment [8]. In [9], a parametric study on the influence of crack face friction and crack position in relation to the sleepers on SIF evolution during a wheel passage is performed for a head check and a squat. The effect of creepage on SIFs for a surface-initiated RCF crack is investigated in [10,11].

Crack growth direction and rate in railway rails are seldom investigated in the literature, and are then mainly studied for 2D models. The influence of tractive forces, crack face friction, crack inclination and plastic stresses is investigated in 2D in [12]. The effect of varying operational loads and crack face friction is studied in [13,14]. The influence of tractive forces and crack face friction is investigated in [15]. However, uncertainties in predicting crack growth direction and rate remain, especially in 3D.

To fill this gap, this study establishes and employs a 3D numerical framework to investigate crack growth in terms of growth direction and rate for a head check under operational loading scenarios. For this, a 3D rail part is considered in Finite Element (FE) simulations. A semi-circular surface-breaking inclined stationary gauge corner crack with frictionless crack faces is modelled using the eXtended Finite Element Method (XFEM). The rail is assumed to behave linearly elastic and the FE model is subjected to combinations of wheel–rail contact load, tensile thermal load, and rail bending. The crack growth direction is predicted using an accumulative Vector Crack Tip Displacement (VCTD) criterion developed for 2D applications in [14], which is based on the original VCTD criterion in [16]. Paris-type equations are used to estimate the crack growth rate, extending the proposed strategy in [14] to account for mode III loading. Results are evaluated at three points along the crack front for four different crack radii and two crack plane inclinations.

The focus of this study is on the influence of different operational loads on the crack growth direction and rate. Criteria for such predictions have previously been developed and validated in [14]. An extension to 3D modelling can be done using explicit crack modelling techniques such as XFEM. As alternatives, peridynamic theories [17] and phase-field methods [18] could be employed. However, with such choices, previously developed criteria would have to be reformulated in the context of crack development in these methods.

The novelty of the research lies in investigating crack growth behaviour in 3D simulations, considering the 3D wheel–rail contact load in combination with thermal and bending loads, and predicting crack growth directions and rates along the crack front under these conditions.

2. Numerical framework

2.1. FE model

The FE model of the rail section features a 300 mm long and 172 mm high 60E1 rail profile with the dimensions in [19], see Fig. 1a. The bottom surface is clamped in the lateral and vertical directions (global x- and y-directions, respectively). Boundary conditions on the vertical side surfaces vary depending on the applied load as described in Section 2.2. The rail section is discretised using standard first-order hexahedral (8-noded brick) elements. The rail material is assumed to be linearly elastic with an elastic modulus of $E = 210$ GPa and a Poisson's ratio of $\nu = 0.3$.

A (quasi) semi-circular crack with varying radius, r, and inclination is considered. The inclined surface-breaking crack is located at the rail gauge corner, see Fig. 1. It is modelled as a stationary crack in ABAQUS/CAE [20] using XFEM [21,22] to circumvent the necessity of aligning the FE mesh with the crack geometry and thereby allowing an identical FE mesh to be used for all investigated cases. This removes comparative discretisation errors. Since XFEM still needs fine mesh around the crack, mesh refinement with elements of 0.4 mm side lengths are employed close to the crack, as shown in Fig. 1. Following field observations in [3], the centre of the crack is located at $(x, y, z) = (-26.0, -2.3, 150.0)$ mm in the global coordinate system of Fig. 1. As shown in Fig. 2, the crack plane has an inclination of φ w.r.t. the z-axis and β w.r.t. the x-axis. For implementing the presumed crack in ABAQUS/CAE, an inclined plane with the desired inclination is incorporated into the FE model, see Fig. 1a, and the crack area shown in Fig. 1b is chosen for considering enrichments in the XFEM formulation. Crack closure constraints are applied using a penalty formulation while the crack face is considered to be frictionless.

2.2. Load scenarios

The studied loads are wheel–rail contact, rail bending, and loading caused by restricted thermal contraction.
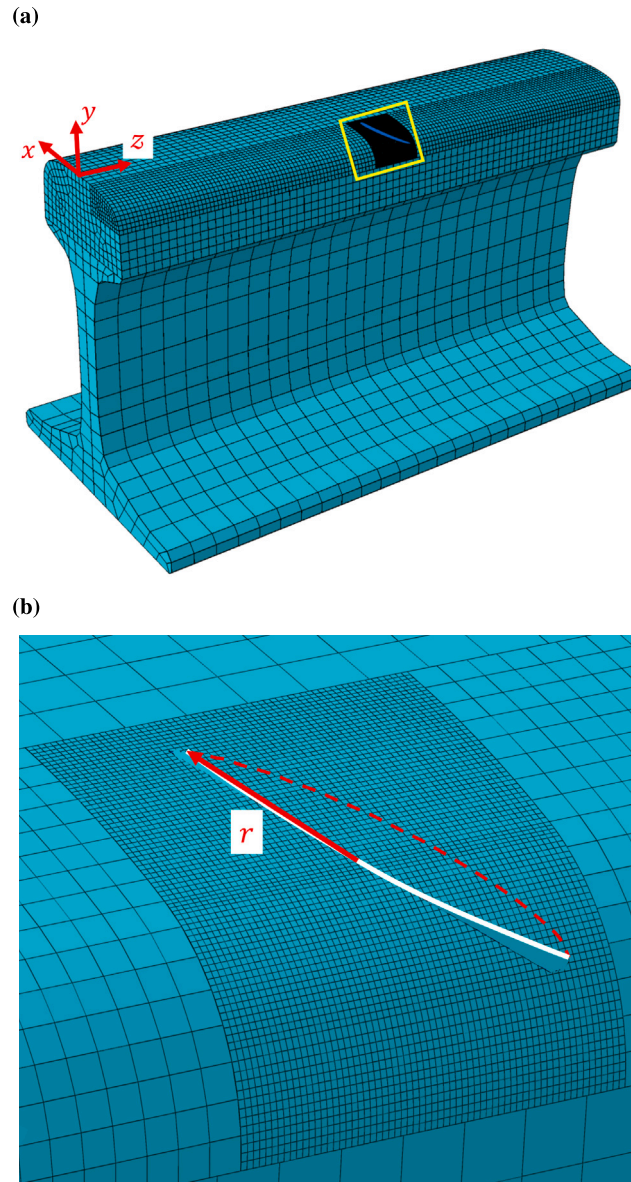
(a)

(b)

Fig. 1. FE mesh for the 60E1 rail profile. (a) Rail model with a semi-circular surface-breaking inclined gauge corner crack. The global Cartesian (x, y, z) coordinate system is indicated. (b) Area around the crack of radius r (marked with a box in (a)). The element size in the crack area is $0.4\,\text{mm}$.

2.2.1. Contact load

Both contact pressure and traction in the wheel–rail contact interface are considered. The wheel–rail normal contact is modelled using Hertzian theory, which gives an elliptical contact patch and pressure distribution between the contacting bodies. Assuming a contact patch with the semi-axes a in the x-direction and b in the z-direction (see Fig. 3b), the contact pressure distribution for a given wheel load position, $(\bar{x}, \bar{z})$, is expressed as

$$p(\bar{x}, \bar{z}; x, z) = \begin{cases} \frac{3P}{2\pi ab}\sqrt{1 - (\frac{x-\bar{x}}{a})^2 - (\frac{z-\bar{z}}{b})^2} & \text{for} \quad (\frac{x-\bar{x}}{a})^2 + (\frac{z-\bar{z}}{b})^2 \leq 1 \\ 0 & \text{for} \quad (\frac{x-\bar{x}}{a})^2 + (\frac{z-\bar{z}}{b})^2 > 1 \end{cases}. \tag{1}$$

Here, P is the vertical wheel load. The semi-axes a and b are evaluated following [23], assuming a wheel with a (rolling) radius of $0.46\,\text{m}$ in contact with a (transverse) rail of head radius $0.3\,\text{m}$ having the same elastic properties. The $0.3\,\text{m}$ radius of the rail head is used for contact patch calculations instead of the gauge corner radius for a nominal profile $(0.080\,\text{m})$ since the latter will increase during operational use due to wear and grinding. This also causes the contact to be shifted more towards the rail head. The
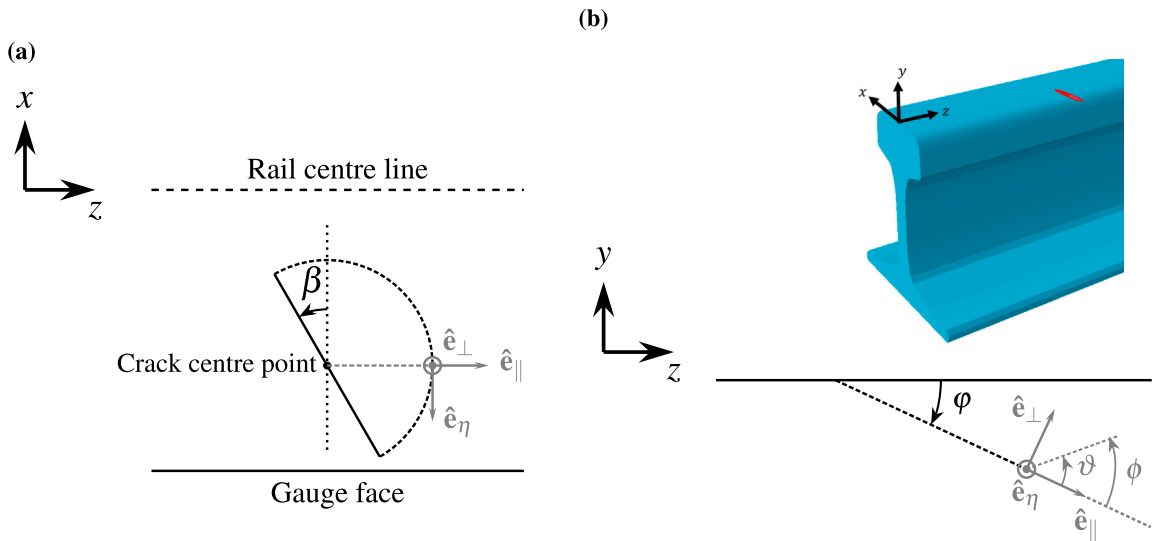
(b)

(a)

Fig. 2. Crack plane orientation w.r.t. the rail. The crack local coordinate system ($\hat{e}_\parallel$, $\hat{e}_\perp$, $\hat{e}_\eta$) for an arbitrary point along the crack front is shown. (a) Top view (xz-plane). (b) Side view of the cracked rail head (yz-plane).

Hertzian pressure is applied as vertical traction on the curved rail surface. The wheel–rail tractive forces in the z-direction, T_z, are evaluated presuming full slip conditions with a traction coefficient f_{wr}, i.e., $T_z = f_{wr}\, P$. Lateral tractive forces (global x-direction) are neglected in this study.

The current study focuses on head checks, see Section 2.1, which mainly appear in curves where the wheel–rail contact occurs close to the gauge shoulder [3]. Based on multi-body simulation results from [24], the contact load is applied with an offset of $\bar{x} = -19$ mm in the global coordinate system of Fig. 1. Note that the crack origin would be just outside of the contact patch, which would relate to initiation at contact closer to the gauge corner, resulting in crack initiation and wear that shifts contact towards the top of the rail resulting in the employed configuration.

The Hertzian theory presumes constant curvature in the contact area, which is violated at the gauge shoulder [25]. To circumvent this issue, it is assumed that the wheel–rail contact occurs at a plane with constant inclination tangent to the theoretical contacting point, cf. Fig. 3c. The vertical wheel load in Eq. (1) is thus projected on this inclined plane, resulting in normal, p_n, and tangential, p_ξ, stress components. The longitudinal tractive force leads to an additional longitudinal frictional stress component, p_t. It is assumed that each stress component on this plane (p_n, p_ξ, p_t) has an elliptical distribution with semi-axes given by Hertzian theory. The maximum values of the components are evaluated such that the resultant forces correspond to the wheel load, P, and the longitudinal tractive force, T_z, in the global y- and z-directions, respectively.

The contact load is implemented in the FE model as distributed stress components (p_n, p_ξ, p_t), as shown in Fig. 3c, for a given wheel load position ($\bar{x}$, $\bar{z}$). To simulate a wheel passage in the simulations, the centre of the contact load is shifted along the positive z-direction in 100 increments. The majority of the load positions considered are located close to the crack, where the impact on crack deformation is greatest. Note that the longitudinal tractive stress, p_t, is applied in the negative z- direction and will thus open up the rail crack [26] as the load approaches the crack mouth. In addition, the vertical side surfaces of the rail are clamped in the longitudinal direction ($u_z^p = 0$) under the pure contact load.

2.2.2. Rail bending load

A traversing wheel imposes rail bending which may be longitudinal and lateral. In this study, lateral bending is not considered, whereas longitudinal rail bending is quantified using the in-house vertical dynamic vehicle–track interaction analysis code DIFF [27]. For this, a smooth wheel with a 7.5 t load is presumed to travel along a smooth rail at 100 km/h. Characteristics of the ballasted track follow [13]. The evolution of the bending moment at a position above a sleeper, where the crack is located, is computed as a function of wheel load position, $\bar{z}$, see Fig. 4. The wheel load is longitudinally positioned at the centre of the crack at $\bar{z} = 0.15$ m. Note that at a distance of about 1.5 sleeper spacings from the crack ($\bar{z} \approx \pm 1$ m) the wheel will induce uplift at the position of the crack. The corresponding boundary displacements on the vertical side surfaces of the rail section in Fig. 1 are evaluated assuming Euler–Bernoulli beam theory [13] as

$$u_z^p\left(\bar{z}; x, y, \frac{L}{2} \pm \frac{L}{2}\right) = \frac{\pm M(\bar{z})\left[h_c + y\right] L}{2E\, I_x},\tag{2}$$

where $u_z^p(\bar{z}; x, y, z)$ are prescribed displacements at (x, y, z) for load position $\bar{z}$. Here, $M(\bar{z})$ is the bending moment, and L is the length of the considered rail section. Further, $h_c = 0.091$ m and $I_x = 30.5 \times 10^{-6}$ m^4 are vertical distance from top surface of the rail to the neutral axis, and the moment of inertia, respectively [19].
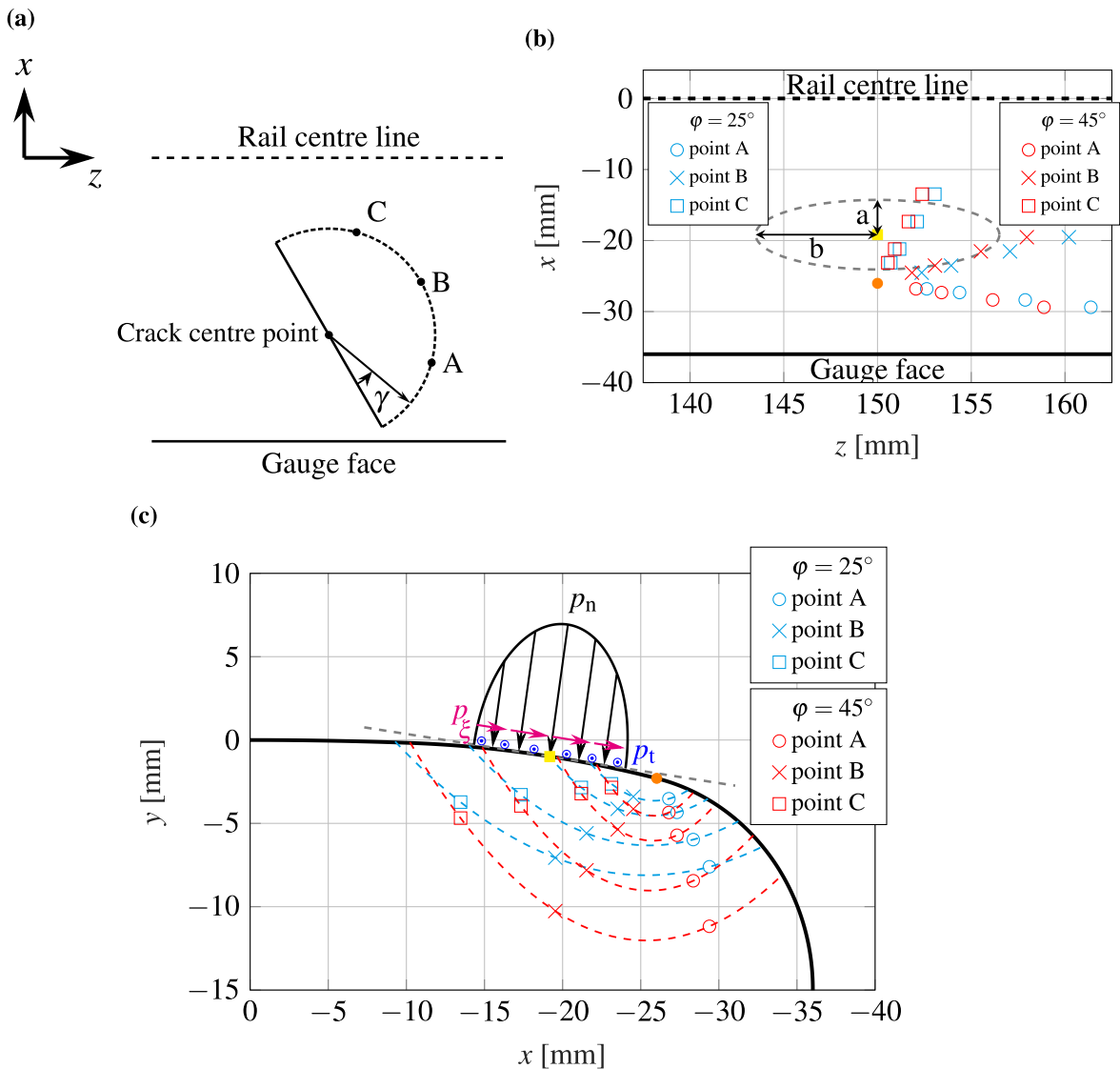
(a)

(b)

(c)

Fig. 3. Evaluation points along the crack front. (a) Points A (gauge side, $\gamma = 45°$), B (centre of crack front, $\gamma = 90°$), and C (field side, $\gamma = 135°$). (b) Top view (xz-plane) for crack radii $r = 3, 5, 9, 13$ mm and all crack plane inclinations. Dashed curve indicates a contact patch with centre marked with a yellow square. The crack centre point for all radii is shown as an orange point. (c) Side view (xy-plane). The grey dashed line shows the tangent plane at the centre of the contact load (marked with a yellow square). The crack centre point for all radii is marked with an orange point.

2.2.3. Thermal load

Temperature variations, $\Delta T = T - T_0$, from the rail stress-free temperature, T_0, induce longitudinal stresses in continuously welded rails due to the restricted contraction. These thermal stresses are quantified employing a linear thermoelasticity assumption, resulting in boundary displacements on the vertical side surfaces [23]

$$u_z^p(x, y, \frac{L}{2} \pm \frac{L}{2}) = \mp \alpha_r \Delta T \frac{L}{2}, \tag{3}$$

where $u_z^p(x, y, z)$ are the prescribed displacements at (x, y, z), $\alpha_r = 11.5 \times 10^{-6}[1/°C]$ is the thermal expansion coefficient of the rail material and L is the length of the modelled rail section. In this study, the tensile thermal loading ($\Delta T < 0$) is investigated.

2.3. Crack propagation

This study investigates initial crack growth directions and rates for stationary cracks. A displacement-based method proposed in [28] is employed to evaluate Stress Intensity Factors (SIFs). The method is particularly developed for multiaxial load cases, especially those with (large) shear and compressive loads, as is the case for the considered load cases. As shown in [28], the method
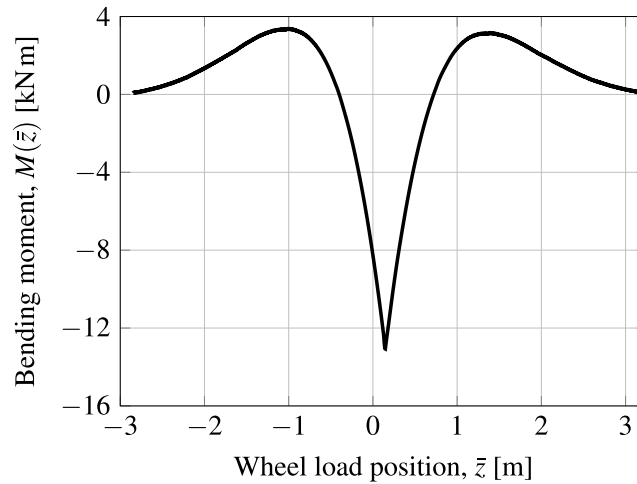
Fig. 4. Evolution of bending moment at the position of the crack mouth as a function of the relative position of the wheel. Results from the vehicle–track simulation using DIFF [27].

captures the evolution of K_{I} better than the J-integral method under rolling contact conditions and is more numerically stable. However, it should be used with caution close to free surfaces due to the implicit presumption of plane strain conditions. The SIF evaluation method has been validated for pure contact load in [28]. For further validation, SIF calculations for a vertical surface-breaking semi-circular gauge corner crack under pure thermal and pure bending loads were compared against analytical formulae in [29]. SIFs for a semi-elliptic crack under pure contact load were also qualitatively compared with available solutions in [30]. In addition, a mesh sensitivity analysis is presented in Appendix.

2.3.1. Initial crack growth direction

Very few criteria in the literature deal with predicting crack growth direction for general 3D mixed-mode loading, since for predominantly tensile loading the crack tends to deviate to mode I. Sih [31] proposed that the crack grows in the direction that minimises the strain energy density function, which is a function of SIFs in all three modes. This minimum always occurs in a plane featuring a zero 'out-of-plane' direction.[1] In other words, the criterion does not consider the influence of mode III on the final growth direction. Pook [32,33] suggested one growth direction as a function of SIFs in modes I and II, and another which also considers mode III. Schöllmann et al. [34] developed a criterion based on the idea that crack propagation occurs perpendicular to the direction of the maximum principal stress with two relations proposed to predict growth directions accordingly. Richard et al. [35] used two relations to predict growth directions, both considering the influence of all three modes. These criteria (and their modifications) were mainly verified for experiments under proportional loading.

There exist a few criteria in 2D for non-proportional loading. The performance of five different criteria under proportional and non-proportional mixed-mode loading for 2D cases were evaluated in [36]. It was found that an accumulated VCTD criterion provided predictions that matched experimental results best under stable shear growth, for the transition from shear to tensile growth, and during tensile growth. All these phenomena may happen in an RCF crack growth. The criterion also has good performance in simulating twin disc experiments [14,37]. Moreover, the predicted crack growth directions on the rail surface using the criterion have a good match with field observations [11]. Therefore, the accumulated VCTD criterion proposed in [36] and modified in [14] is chosen and employed under 3D conditions in the current study. The criterion considers only the influence of modes I and II. There is a lack of (large) experimental data in the literature to assess the performance of the criterion under a general 3D case of non-proportional loading, involving all three modes. In this study, any potential influence of mode III on the crack growth direction is thus discarded.

For the accumulated VCTD criterion, the crack face opening displacement, $\delta_{\mathrm{I}}(t)$, and crack face sliding displacement, $\delta_{\mathrm{II}}(t)$, are computed at each time instance t of the load cycle. As choosing the evaluation points for a crack in 3D is not as unambiguous as in 2D where there is only a crack line with a tip, the VCTD predictions employ crack face displacements evaluated from SIFs. Following [38], crack face displacements are calculated as the difference between the top and bottom surface crack face displacements ($\vartheta = \pi$, and $\vartheta = -\pi$, respectively) at a distance d from the crack tip using the displacement fields in the vicinity of the crack tip, expressed in the crack local coordinate system shown in Fig. 2b, and under plane strain conditions. By defining a factor $B(d) = \frac{8(1-\nu^2)}{E}\sqrt{\frac{d}{2\pi}}$, the crack face opening, $\delta_{\mathrm{I}}(d,t)$, and sliding, $\delta_{\mathrm{II}}(d,t)$, displacements are thus

$$\delta_{\mathrm{I}}(d,t) = u_\perp(d,\pi,t) - u_\perp(d,-\pi,t) = B(d)K_{\mathrm{I}}(t),$$
$$\delta_{\mathrm{II}}(d,t) = u_\parallel(d,\pi,t) - u_\parallel(d,-\pi,t) = B(d)K_{\mathrm{II}}(t).$$

$$(4)$$

---

[1] Here, the out-of-plane direction refers to the direction that involves mode III SIF influence.

In this study, $d = 1$ mm is used and negative values of $K_I(t)$ are truncated to remove the influence of minute crack face penetrations that occur in numerical simulations. Further, the 'amplitudes' of $\delta_I(t)$ and $\delta_{II}(t)$ are defined as

$$\tilde{\delta}_{I/II}(t) = \delta_{I/II}(t) - \overline{\delta}_{I/II}, \tag{5}$$

where $\overline{\delta}_{I/II} = \frac{1}{2}\left[\max_t\left(\delta_{I/II}(t)\right) + \min_t\left(\delta_{I/II}(t)\right)\right]$ are mid-values over the load cycle.

The crack driving displacement vector, $\Delta\mathbf{c}$, is evaluated based on the 'rate-independent' response over the load cycle

$$\Delta\mathbf{c} = \int_0^{T_c} \langle \frac{d\delta_a(t)}{dt} \rangle \hat{\mathbf{e}}_\vartheta(t)\, dt. \tag{6}$$

Here, T_c is the duration of the load cycle, and $\langle \bullet \rangle := \frac{1}{2}(\bullet + |\bullet|)$ are Macaulay brackets. The instantaneous crack driving displacement, $\delta_a(t)$, is evaluated as

$$\delta_a(t) = \sqrt{\langle\tilde{\delta}_I(t)\rangle^2 + 2\langle\tilde{\delta}_I(t)\rangle|\tilde{\delta}_{II}(t)| + 2\tilde{\delta}_{II}(t)^2}. \tag{7}$$

Further, $\hat{\mathbf{e}}_\vartheta$ is the unit vector in the direction of the instantaneous crack growth direction, $\vartheta(t)$, see Fig. 2b. The instantaneous crack growth direction is computed as

$$\vartheta(t) = \arcsin\left(\frac{-\tilde{\delta}_{II}(t)}{\delta_a(t)}\right). \tag{8}$$

The accumulated crack propagation direction for the entire load cycle, ϕ, in the crack local coordinate system of Fig. 2b is computed as a unit vector in the direction of the crack driving displacement vector $\Delta\mathbf{c}$, i.e.,

$$\hat{\mathbf{e}}_\phi = \frac{\Delta\mathbf{c}}{\|\Delta\mathbf{c}\|}. \tag{9}$$

2.3.2. Crack growth rate

In the case of non-proportional loading, the phase angle between the modes varies over time. This can be considered by either developing an accumulation scheme based on instantaneous contributions (similar to the employed criterion for the crack growth direction in Section 2.3.1), or by estimations using existing in-phase growth laws. The former has the complication of requiring an accumulation scheme which demands (extensive) experimental data for calibration.

Paris law [39] is one of the most widely employed growth laws in predicting crack growth rate in uniaxial fatigue. It relates the crack growth rate, da/dN, to the range of the SIF, ΔK, with a power law as $da/dN = C(\Delta K)^m$. Here, C and m are material parameters evaluated from experiments.

In the current study, Paris law is extended to two exponential relations to consider different mode interactions. Following the idea proposed in [40] for modes I and II, the loading is first presumed to be sequential without any mode overlap. This assumption gives a lower estimate for the growth rate as it does not consider any interactions between the modes. The total growth rate is thus calculated from the sum of the contribution of the three modes, i.e.,

$$\left(\frac{da}{dN}\right)_{lo} = C(\Delta K_I)^m + C(\Delta K_{II})^m + C\left(\frac{\Delta K_{III}}{\sqrt{1-\nu}}\right)^m, \tag{10}$$

where ν denotes the Poisson's ratio. Here, the material parameters, C and m, are taken the same for all three modes.[2]

Alternatively, the loading is presumed to be applied simultaneously, which gives an upper estimate of the crack growth rate

$$\left(\frac{da}{dN}\right)_{up} = C(\Delta K_{eq})^m. \tag{11}$$

Here, ΔK_{eq} is the equivalent SIF derived from the energy release rate under plane strain conditions, defined as [41]

$$\Delta K_{eq} = \sqrt{\Delta K_I^2 + \Delta K_{II}^2 + \frac{1}{1-\nu}\Delta K_{III}^2}. \tag{12}$$

In this study, $C = 2.47 \times 10^{-9} \frac{\text{mm/cycle}}{(\text{MPa}\sqrt{\text{m}})^m}$ and $m = 3.33$ are employed, which corresponds to mode I propagation in rail steel UIC grade 900A [42].

3. Analyses and results

3.1. Preliminaries

The FE model described in Sections 2.1 and 2.2 was implemented in ABAQUS/CAE [20]. Post-processing following Section 2.3 was carried out in MATLAB [43]. Predicted growth directions and rates were evaluated at three different points along the crack front as shown in Fig. 3a. Four different crack radii ($r = 3, 5, 9, 13$ mm) and two crack plane inclinations were included in the

---

[2] The assumption is employed as the current study focuses on the qualitative comparison of the predicted crack growth rates under different load scenarios. The authors are aware that the employed assumption causes some inaccuracies in quantitative rate predictions.

study. Motivated by field observations in [3,44,45], the crack plane was assumed to have an orientation with $\varphi = 25°$ and $\beta = 27°$, see Fig. 2, (labelled as '$\varphi = 25°$' henceforth). As a comparison, an orientation with $\varphi = 45°$ and $\beta = 21°$ (denoted '$\varphi = 45°$') was considered. The crack is not propagated in this study. Rather, the situation is analysed for varying sizes of assumed cracks. The reason is that the different directions and rates predicted along the crack front would require significant assumptions on how intermediate points are affected, and how the twisted crack front would affect further propagation. The predicted crack growth directions are presented in the crack local coordinate system in terms of direction ϕ (see Fig. 2b). Here, $\phi = 0$ corresponds to the initial slope of the crack, $\phi > 0$ implies kinking upwards, and $\phi < 0$ implies a tendency to grow downwards from the initial crack plane.

3.2. Contact load

A pure contact load resulting from a 7.5 t wheel load with a traction coefficient f_{wr} was applied. Semi-axes of the contact patch were evaluated as $a = 4.9$ mm and $b = 6.5$ mm. The vertical side surfaces of the rail were clamped in the longitudinal direction of the rail ($u_z^p = 0$). Two cases were studied for this load: no tractive force, $f_{wr} = 0$, and $f_{wr} = 0.3$. The projected (peak) contact stresses (see Fig. 3c) were computed as $(p_n, p_\xi, p_t) = (1091, 161, 0)$ MPa, and $(p_n, p_\xi, p_t) = (1091, 161, 331)$ MPa, respectively.

Figs. 5a and 6 show predicted growth directions and rates for $f_{wr} = 0$ and a crack plane inclination of $\varphi = 25°$. Similar to the illustrated results in Fig. 7, it is found that instances with a contact load far away from the crack mainly propagate downwards while upward kinking is generally promoted when the contact load is close to the crack. As the influence of the contact is much higher in the vicinity of the crack, the overall expected behaviour for this case is upward growth. Fig. 5a generally reflects this expectation for all three points along the crack front, with exceptions for $r = 9$ mm, points B and C. This deviation is likely due to their location (almost) under the contact load peak, see Fig. 3c, which generates a severe crack closure. Even though the contact constraints are only applied in the crack local normal direction ($\hat{e}_\perp$ in Fig. 2b), also the general sliding behaviour of the points is affected due to the restricted movement. This limits contributions from instances when the contact load is close to the crack, which promotes upward kinking.

The predicted crack growth rates in Fig. 6 increase as the crack radius increases from $r = 3$ mm to $r = 9$ mm. This is caused by a closer distance to the contact load (and its peak) for points B and C, and is (likely) a consequence of the larger crack size and boundary effects for point A. For $r = 13$ mm, points B and C are located further away from the contact load, see Fig. 3c. This leads to a reduction of the crack growth for point C and a smaller increase for point B. It should be noted that point A has a lower crack growth rate compared to the two other points as it is further from the contact load. Both lower (Eq. (10)) and upper (Eq. (11)) growth rate estimates show the same trends.

Adding a tractive force that opens up the crack mouth can promote more downward growth. This behaviour is generally observed by comparing the predicted directions in Fig. 5b to those in Fig. 5a. The exceptions to this trend are points B and C for $r = 9$ mm, which kink slightly more upwards. A possible reason for this is that the tractive force opens up some of the crack closure that occurs at time instances with upward kinking. It is seen that the influence of the tractive force decreases for larger cracks. Comparing the predicted rates in Figs. 8b and 8a shows that predicted growth rates are higher for smaller cracks, $r \leq 5$ mm, in the presence of tractive forces, but otherwise follow similar trends as without traction.

The same investigations were performed for a crack plane inclination of $\varphi = 45°$. For a case of $f_{wr} = 0$ (Fig. 9a), the results generally show kinking upwards, with some deviations. As before, point C for $r = 9$ mm kinks downwards. This point is very close to the corresponding point for a crack plane inclination of $\varphi = 25°$, see Fig. 3c. Also, at point B for $r = 5$ mm the tendency is downwards. A possible reason is the crack closure around this point as motivated by the similar locations of point B for $r = 5$ mm with $\varphi = 45°$ and point B for $r = 9$ mm with $\varphi = 25°$, see Fig. 3c.

The steeper crack plane inclination reduces the influence of a contact load close to the crack since the crack front is deeper below the contact. The complex interaction of this effect and the influence of crack size can be the cause of downward crack growth for points A and B of the smallest crack. Predicted growth rates in Fig. 10a show the same trend as results for $\varphi = 25°$ (Fig. 8a) with generally lower rates. This is expected due to the steeper inclination of the crack plane.

Adding a tractive force generally promotes more downwards crack growth also for $\varphi = 45°$, see Fig. 9b. For points with severe crack closure (e.g., point B for $r = 5$ mm and point C for $r = 9$ mm), traction releases some of the crack closure, which can lead to higher contribution of upward kinking and shallower crack growth directions. This phenomenon, i.e., releasing some of the crack closure and thereby allowing more contribution of contact load close to the crack, also happens for point A for $r = 13$ mm. Predicted growth rates in Fig. 10b follow the trend seen for $\varphi = 25°$ (Fig. 8b) with generally lower rates.

3.3. Combined thermal and contact load

A combination of a 7.5 t wheel load with $f_{wr} = 0.3$ and a thermal load corresponding to $\Delta T = -20°$C was considered. The thermal load was applied as boundary displacements evaluated from Eq. (3), and the contact load parameters followed Section 3.2. As motivated in [14], mid-values of crack face displacements over a load cycle (Eq. (5)) need to be computed solely from the contact load (i.e., in a separate simulation) due to the difference in the length of the thermal and contact load cycles that will affect the kinematic hardening around the crack front. In essence, the many contact load cycles during one thermal cycle will shakedown the contact stress response, but not the thermal response. Removing the shakedown mid-value is called $\bar{\delta}$-correction henceforth.

It is observed that the crack under a pure thermal load cycle (not shown here) tends to grow downwards. Crack growth rates increase as the crack radius increases, but are low.
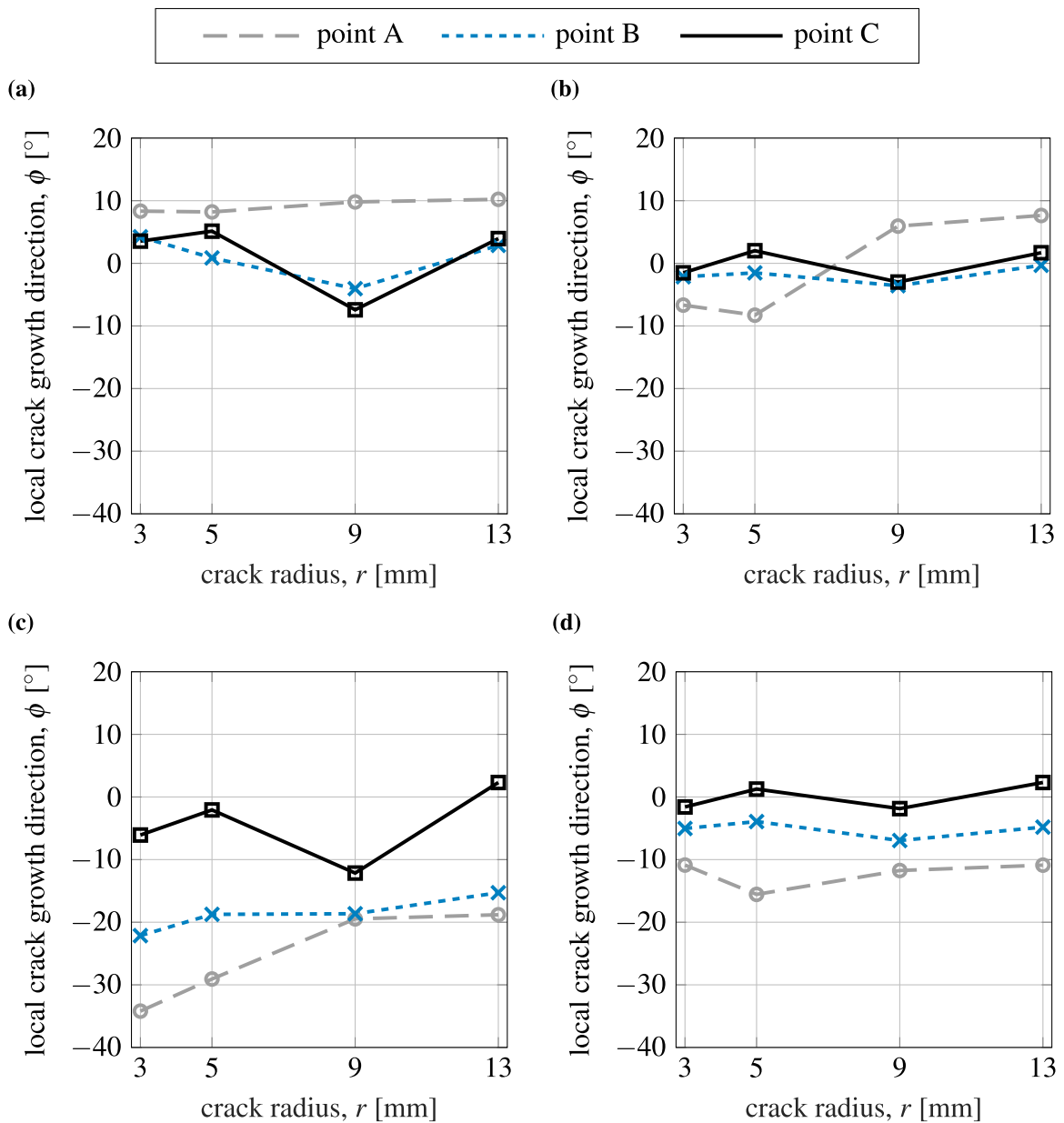
Fig. 5. Predicted growth directions, $\varphi = 25°$. (a) Pure contact, 7.5 t wheel load, $f_{wr} = 0$. (b) Pure contact, 7.5 t wheel load, $f_{wr} = 0.3$. (c) Thermal ($\Delta T = -20\,°C$) and 7.5 t wheel load, $f_{wr} = 0.3$, with $\bar{\delta}$-correction. (d) Bending and 7.5 t wheel load, $f_{wr} = 0.3$.

Fig. 5c shows predicted growth directions under combined thermal and contact load for a crack plane inclination of $\varphi = 25°$. Note that the $\bar{\delta}$-correction was applied for this combined load. It is seen that adding a tensile thermal load promotes more downward growth. The only outlier here is point C in $r = 13\,mm$, which kinks upwards slightly more than under pure contact load. The likely cause is the increased crack opening due to the additional thermal load, which gives a slightly higher contribution from instances with upward kinking during a load cycle. The influence of the thermal load is highest in point A. Predicted growth rates for combined thermal and contact load in Fig. 8c follow the same trend as for the pure contact load (Fig. 8b) with slightly higher values due to the addition of a (quasi-static) tensile crack loading from the thermal load.

Predicted growth directions under combined thermal and contact load for $\varphi = 45°$, shown in Fig. 9c, are more downward than for pure contact (Fig. 9b). The only deviation is point C for $r = 13\,mm$ (same effect as for $\varphi = 25°$). Also, predicted growth rates for $\varphi = 45°$ in Fig. 10c follow the trend of $\varphi = 25°$ (Fig. 8c) and with generally lower values. A larger difference between the combined load and pure contact (Fig. 10b) is seen due to the larger influence of thermal load for steeper cracks, especially in point A, where the relative influence of the thermal load is the highest.
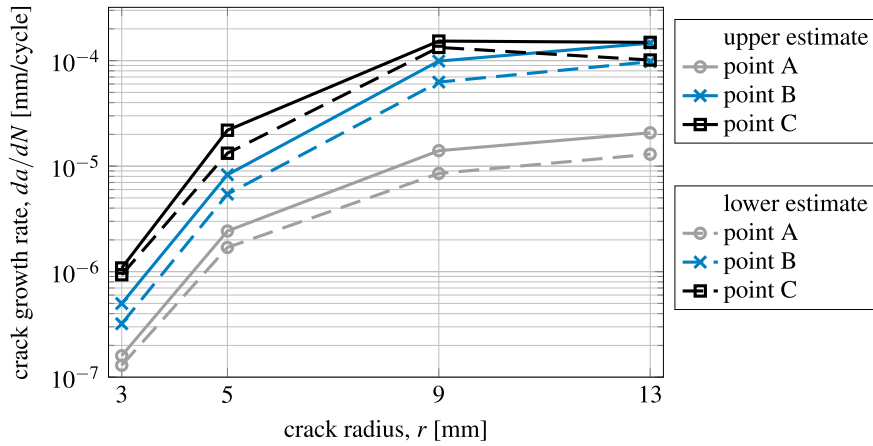
Fig. 6. Predicted growth rates along the crack front of a frictionless semi-circular gauge corner crack with $\varphi = 25°$ under a 7.5 t wheel load with $f_{wr} = 0$.
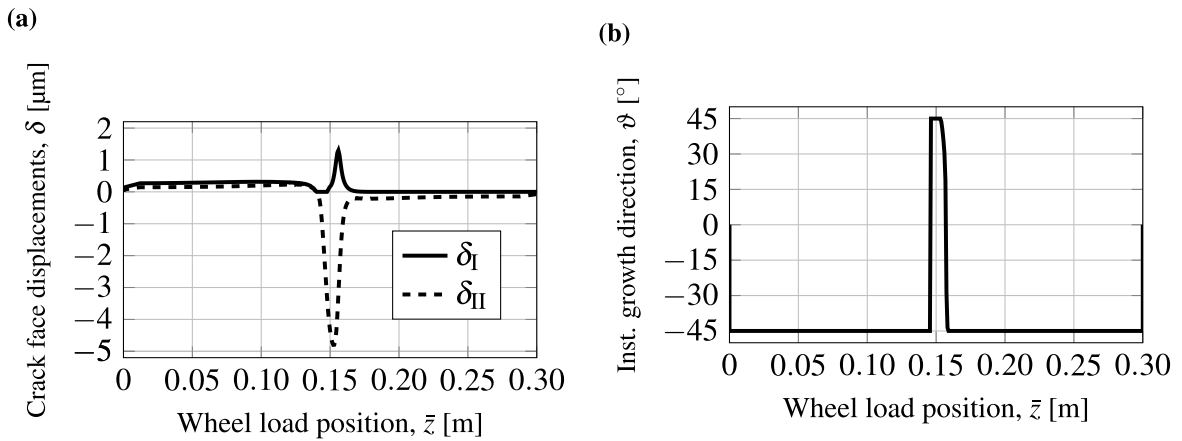
(a)

(b)

Fig. 7. Evolution of the parameters over a load cycle for point C of a frictionless semi-circular gauge corner crack with $r = 5$ mm and $\varphi = 25°$ under a 7.5 t wheel load with $f_{wr} = 0$. (a) Crack face displacements. (b) Instantaneous growth direction.

3.4. Combined bending and contact load

A combination of bending and a 7.5 t wheel load with $f_{wr} = 0.3$ was studied. The bending was applied as boundary displacements following Eq. (2). The contact load parameters followed Section 3.2.

The crack grows downwards under pure bending (not shown here) for all points along the crack front with the same trend for crack plane inclinations $\varphi = 25°$ and $\varphi = 45°$. Predicted growth rates increase as the crack radius increases, and are higher for the $\varphi = 45°$ case. This is expected due to the higher influence of the longitudinal bending stress for the steeper crack. However, crack growth rates under pure bending loading are low.

Predicted growth directions under combined bending and contact for $\varphi = 25°$ are shown in Fig. 5d. Note that, the $\bar{\delta}$-correction (see Section 3.3) is not adopted for this combined load case as the length of contact and bending load cycles are on the same order [14]. Adding the described bending load to the pure contact load results in additional tensile loading at both ends of the load cycle (as a far-field load in the absence of the contact load), see Fig. 4. This means that this combined load can promote more downward growth than pure contact load. Comparison of results in Figs. 5d and 5b reflects this expectation with a minor deviation for point C in $r \geq 9$ mm. This is likely because the additional compressive load from the bending increases the crack displacements for upward kinking instances, especially for $r = 9$ mm. As discussed in Section 3.2, point C experienced severe crack closure under pure contact load, and the compressive bending load can slightly increase the sliding displacements for upward kinking instances. The bending load has the most influence in point A. Predicted growth rates for the combined load in Fig. 8d are very close to pure contact load values (Fig. 8b).

To compare the rate predictions with field measurements, [46] reports head check crack growth of about 1 mm in depth per 100 Mega Gross Tonnes (MGT) of traffic using eddy current and alternating current potential drop measurements. Considering a crack with $\varphi = 25°$ and assuming steady-state crack growth, i.e., $\Delta a = \frac{da}{dN} \Delta N$, the predicted rates for point B under combined bending and contact for $r = 3$ mm give a passing traffic range of 17 MGT $\leq$ traffic $\leq$ 23 MGT for 1 mm crack growth in depth with an axle load
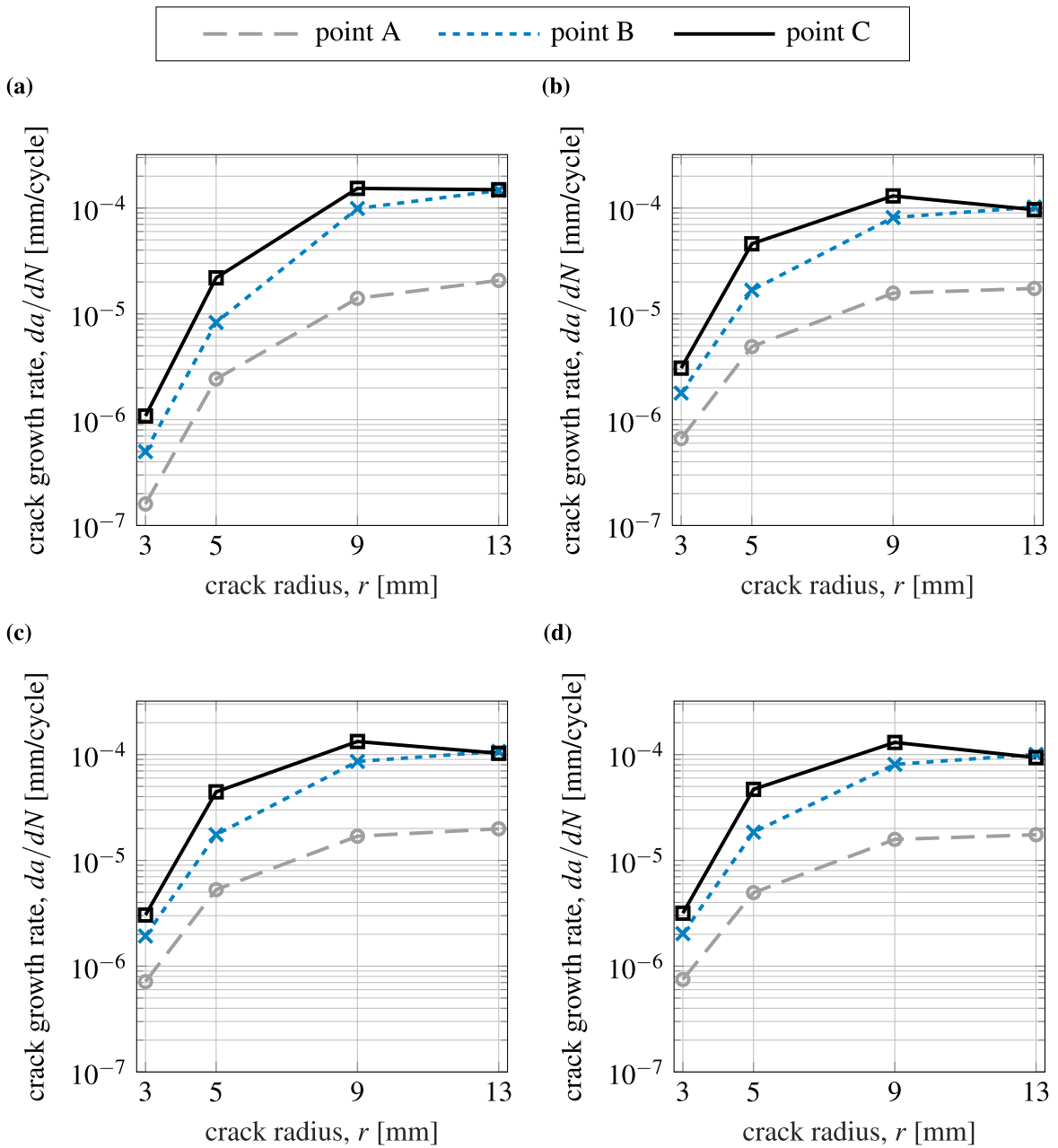
Fig. 8. Upper estimate of predicted growth rates, $\varphi = 25°$. (a) Pure contact, 7.5 t wheel load, $f_{wr} = 0$. (b) Pure contact, 7.5 t wheel load, $f_{wr} = 0.3$. (c) Thermal ($\Delta T = -20\,°C$) and 7.5 t wheel load, $f_{wr} = 0.3$. (d) Bending and 7.5 t wheel load, $f_{wr} = 0.3$.

of 15 t. Using rates evaluated for point A gives a passing traffic range of 47 MGT $\leq$ traffic $\leq$ 71 MGT. Faster growth is thus being predicted by simulations than field measurements. Note however that crack face friction and residual stresses were not included in the simulations. Crack face friction may have a significant influence on crack growth rates [7]. In addition, neglecting compressive residual stresses that under normal conditions occur close to the rail surface leads to conservative (i.e., higher) crack growth rate predictions in the simulations [7,12]. The order of crack growth rates in the predictions can thus be considered reasonable for the current qualitative investigations.

Simulations featuring $\varphi = 45°$ (Fig. 9d) show similar trends as for $\varphi = 25°$. Similar to the case of $\varphi = 25°$, the additional compressive bending load in the presence of the contact load can increase crack displacements for instances with upward kinking. This effect is more pronounced for $\varphi = 45°$ due to the higher influence of compressive bending stress on the steeper crack plane.
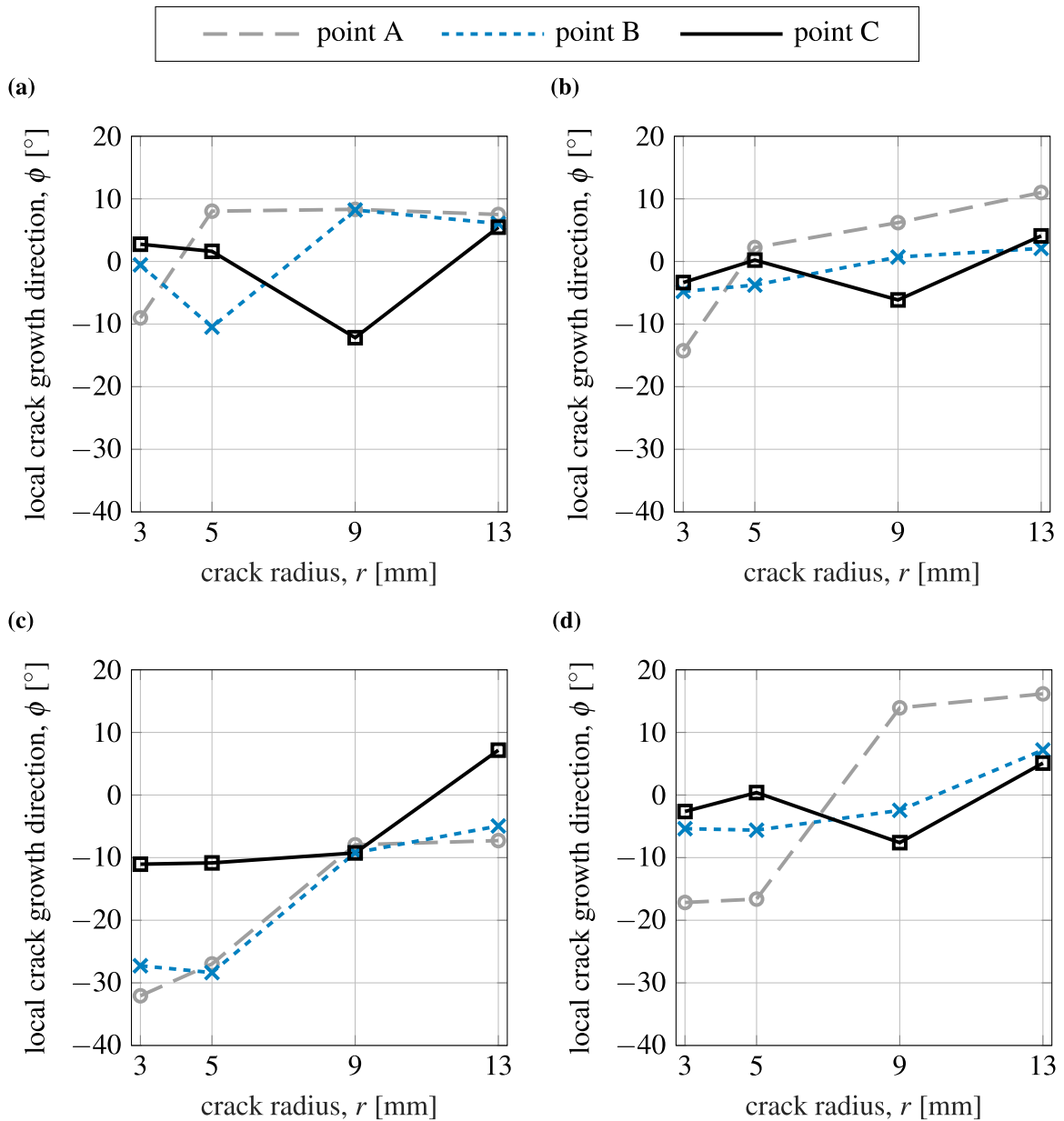
Fig. 9. Predicted growth directions, $\varphi = 45°$. (a) Pure contact, 7.5 t wheel load, $f_{wr} = 0$. (b) Pure contact, 7.5 t wheel load, $f_{wr} = 0.3$. (c) Thermal ($\Delta T = -20\,°C$) and 7.5 t wheel load, $f_{wr} = 0.3$, with $\bar{\delta}$-correction. (d) Bending and 7.5 t wheel load, $f_{wr} = 0.3$.

Predicted growth rates presented in Fig. 10d also follow the trend for $\varphi = 25°$ (Fig. 8d) with generally lower rates (and close to values for pure contact).

4. Conclusions and outlook

A numerical framework for the prediction of RCF crack growth in a rail head has been developed. For this, a 3D elastic model of a rail section with a 60E1 rail profile featuring an inclined surface-breaking semi-circular stationary gauge corner crack with frictionless crack faces is considered. SIF evolutions over one load cycle are evaluated and used for predicting crack growth directions and rates. The crack growth direction is evaluated using an accumulative VCTD criterion and crack growth rates are estimated using two Paris-type equations. Four different crack radii and two crack plane inclinations are considered. Results are evaluated at three points along the crack front.
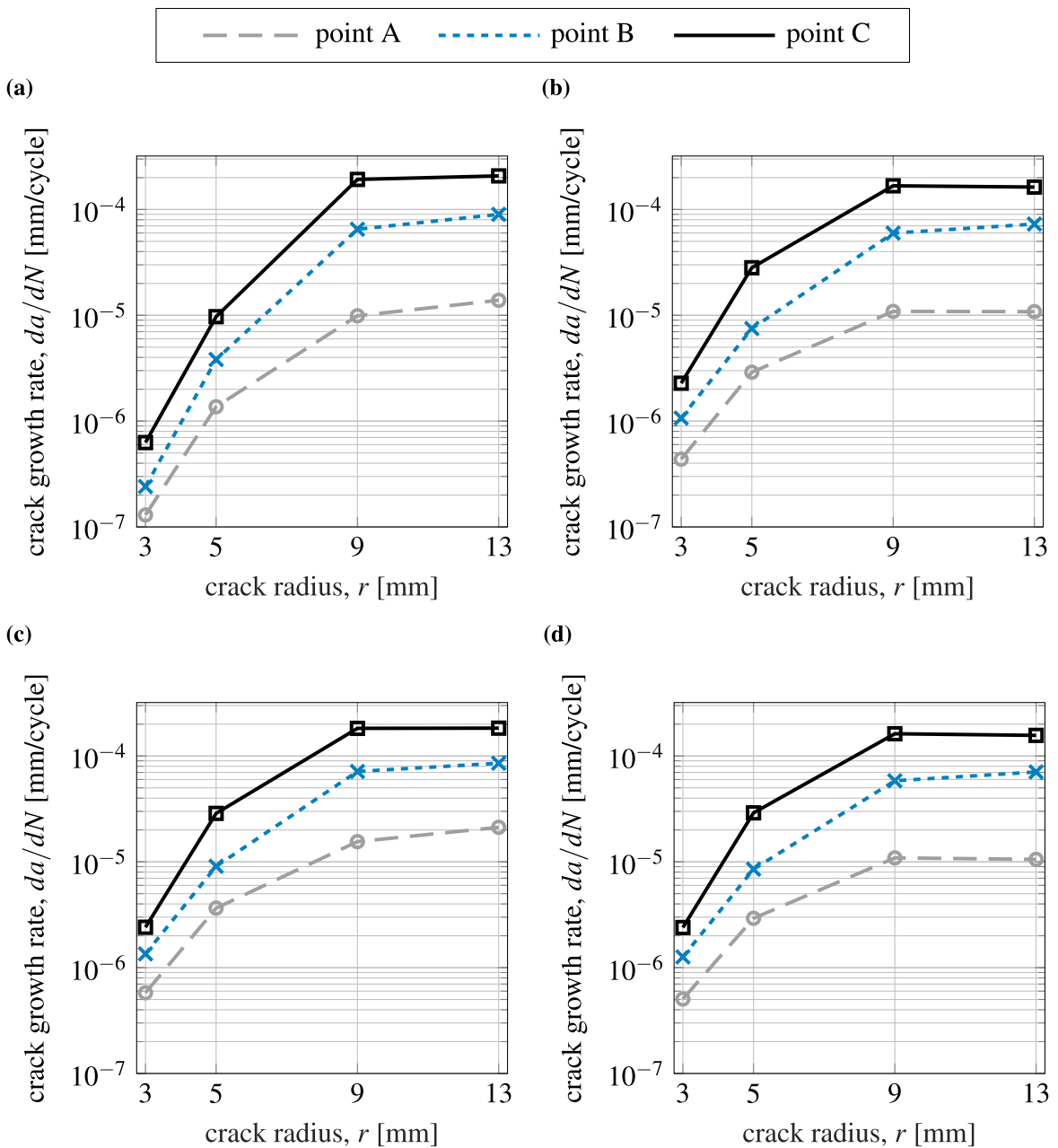
Fig. 10. Upper estimate of predicted growth rates, $\varphi = 45°$. (a) Pure contact, 7.5 t wheel load, $f_{wr} = 0$. (b) Pure contact, 7.5 t wheel load, $f_{wr} = 0.3$. (c) Thermal ($\Delta T = -20\,°C$) and 7.5 t wheel load, $f_{wr} = 0.3$. (d) Bending and 7.5 t wheel load, $f_{wr} = 0.3$.

Growth direction predictions under pure contact load without a tractive force show that the crack mainly tends to kink upwards. Deviations were found to be related to severe crack closure for points located (almost) under the peak of the contact load. Adding a tractive force promotes more downward crack growth. Combined tensile thermal and contact load generally promotes more downward crack growth and reduces crack closure effects. Also, for a combination of bending and contact load, the crack tends to grow downwards. However, in some cases, the crack tends to kink more upwards than under a pure contact load. This is a result of the additional compressive bending load adding to the deformation of the closed crack. The gauge side part of the crack (point A) deviates more from the initial crack inclination under all investigated load cases.

A tractive force generally increases the crack growth rate except for the largest considered radius, $r = 13$ mm. Predicted rates under combined bending and contact are very close to those of pure contact. The predicted crack growth rates are qualitatively

comparable to values from field measurements. For combined tensile thermal and contact load, rates are higher than (but still close to) those of pure contact. For all investigated load cases, the crack growth rates are generally lower for a crack plane inclination of $\varphi = 45°$. Predicted rates at the gauge side (point A) are generally lower than for the other two points. This is in line with field observations of rail breaks presented in [47].

The above conclusions were drawn based on the limited number of investigated cases. A sensitivity analysis on the parameters such as load magnitudes and crack location may highlight limitations. A similar 2D numerical framework has been previously verified against a twin-disc experiment in [14]. However, further calibrations in 3D are needed for more precise quantitative predictions.

A frictionless stationary crack was considered in this study. For future studies, simulation of a propagating crack would improve quantitative validations of the predictions against experimental results and field data. However, as mentioned, this introduces significant complications. Considering crack face friction would also add an important factor to understanding the crack growth behaviour. The frictionless assumption adopted here can be justified for the smaller cracks in the field but full lubrication of deeper cracks hardly happens in reality. Further, it is observed in the study that severe crack closure can happen in some cases. This further highlights the importance of considering crack face friction and crack face locking for predictions. Lastly, anisotropy close to the rail surface could have an influence on the crack growth predictions.

CRediT authorship contribution statement

Mohammad Salahi Nezhad: Conceptualization, Methodology, Software, Validation, Writing – original draft, Writing – review & editing. **Fredrik Larsson:** Conceptualization, Methodology, Supervision, Resources, Writing – review & editing. **Elena Kabo:** Conceptualization, Methodology, Supervision, Resources, Writing – review & editing. **Anders Ekberg:** Conceptualization, Methodology, Supervision, Resources, Writing – review & editing.

Declaration of competing interest

The authors declare that they have no known competing financial interests or personal relationships that could have appeared to influence the work reported in this paper.

Data availability

Data will be made available on request.

Appendix. Mesh sensitivity analysis

An FE mesh sensitivity analysis was performed with three element sizes in the crack area for an inclined crack with $\varphi = 25°$. The analysis featured a pure contact load of a 7.5 t wheel load with a tractive force $f_{wr} = 0.3$ (with contact load parameters given in Section 3.2). These FE analyses are carried out for:

- 'fine mesh' with a mesh size of 0.3 mm with 951 396 nodes,
- 'normal mesh' with a mesh size of 0.4 mm with 421 532 nodes (as seen in Fig. 1),
- 'coarse mesh' with a mesh size of 0.6 mm with 155 788 nodes.

The results are presented in Figs. A.1 and A.2. Predicted directions are in general not significantly affected by a mesh refinement. The only notable difference between predictions for normal and fine meshes is for point C with $r = 3$ mm, which has a difference of about 3°. The difference for the remaining cases is below 2° between these two meshes. The rate predictions also show similar results between normal and fine mesh. Note that the convergence in the results is more pronounced with increasing crack radius, which is expected as the smaller cracks are more sensitive to discretisation errors.
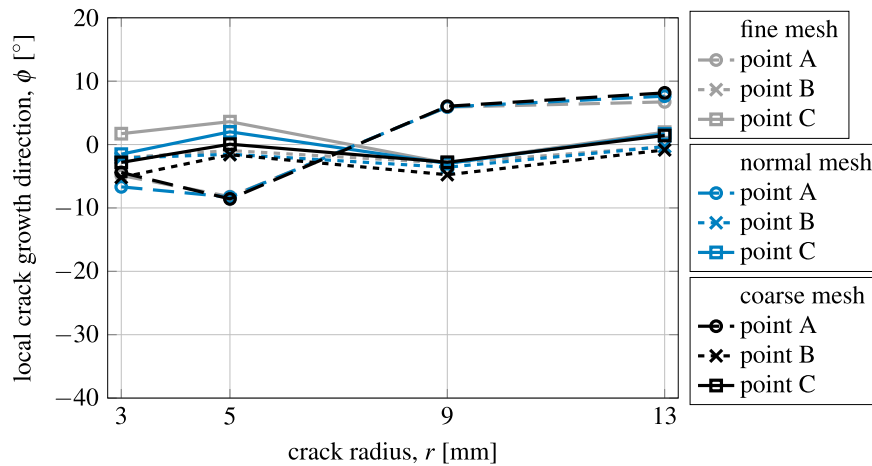
Fig. A.1. Predicted growth directions for three FE meshes along the crack front of a frictionless semi-circular gauge corner crack with $\varphi = 25°$ under a 7.5 t wheel load with $f_{wr} = 0.3$.
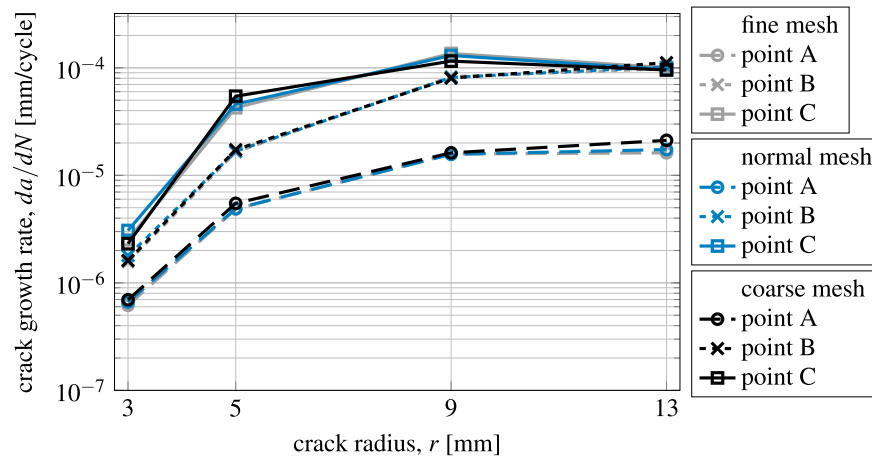

Fig. A.2. Upper estimate of predicted growth rates for three FE meshes along the crack front of a frictionless semi-circular gauge corner crack with $\varphi = 25°$ under a 7.5 t wheel load with $f_{wr} = 0.3$.

References

[1] Doll C, Brauer C, Köhler J, Scholten P. Methodology for GHG efficiency of transport modes. Fraunhofer-Institute for Systems and Innovation Research ISI; 2011, 88 p.

[2] Zerbst U, Lundén R, Edel K-O, Smith RA. Introduction to the damage tolerance behaviour of railway rails – a review. Eng Fract Mech 2009;76(17):2563–601. http://dx.doi.org/10.1016/j.engfracmech.2009.09.003.

[3] Dollevoet RPBJ. Design of an anti head check profile based on stress relief. PhD thesis, University of Twente; 2010, 151 p, http://dx.doi.org/10.3990/1.9789036530736.

[4] IRS 70712: Rail defects. International Union of Railways (UIC), 1st edition, 2018-5; 2018, 115 p.

[5] Bower AF. The influence of crack face friction and trapped fluid on surface initiated rolling contact fatigue cracks. J Tribol 1988;110(4):704–11. http://dx.doi.org/10.1115/1.3261717.

[6] Bogdański S, Olzak M, Stupnicki J. Numerical stress analysis of rail rolling contact fatigue cracks. Wear 1996;191(1):14–24. http://dx.doi.org/10.1016/0043-1648(95)06685-3.

[7] Bogdański S, Olzak M, Stupnicki J. Numerical modelling of a 3D rail RCF 'squat'-type crack under operating load. Fatigue Fract Eng Mater Struct 1998;21(8):923–35. http://dx.doi.org/10.1046/j.1460-2695.1998.00082.x.

[8] Bogdański S, Lewicki P. 3D model of liquid entrapment mechanism for rolling contact fatigue cracks in rails. Wear 2008;265(9):1356–62. http://dx.doi.org/10.1016/j.wear.2008.03.014.

[9] Mai SH, Gravouil A, Nguyen-Tajan ML, Trollé B. Numerical simulation of rolling contact fatigue crack growth in rails with the rail bending and the frictional contact. Eng Fract Mech 2017;174:196–206. http://dx.doi.org/10.1016/j.engfracmech.2016.12.019.

[10] Rodríguez-Arana B, Bergara A, Gil-Negrete N, Nieto J. XFEM rolling contact fatigue crack propagation in railways considering creepages on contact shear stresses. Eng Fract Mech 2022;276:108896. http://dx.doi.org/10.1016/j.engfracmech.2022.108896.

[11] Wu Y, Chung LP, Huang P, Welsby D, Mutton P, Paradowska A, et al. Effect of creepages on stress intensity factors of rolling contact fatigue cracks. Eng Fract Mech 2023;289:109477. http://dx.doi.org/10.1016/j.engfracmech.2023.109477.

[12] Trollé B, Baietto M-C, Gravouil A, Mai SH, Prabel B. 2D fatigue crack propagation in rails taking into account actual plastic stresses. Eng Fract Mech 2014;123:163–81. http://dx.doi.org/10.1016/j.engfracmech.2014.03.020.

[13] Salahi Nezhad M, Floros D, Larsson F, Kabo E, Ekberg A. Numerical predictions of crack growth direction in a railhead under contact, bending and thermal loads. Eng Fract Mech 2022;261:108218. http://dx.doi.org/10.1016/j.engfracmech.2021.108218.

[14] Salahi Nezhad M, Larsson F, Kabo E, Ekberg A. Numerical prediction of railhead rolling contact fatigue crack growth. Wear 2023;530–531:205003. http://dx.doi.org/10.1016/j.wear.2023.205003.

[15] Hengeveld ST, Leonetti D, Snijder B, Maljaars J. Prediction of fatigue crack paths including crack-face friction for an inclined edge crack subjected to mixed mode loading. Procedia Struct Integr 2024;54:34–43. http://dx.doi.org/10.1016/j.prostr.2024.01.053.

[16] Li C. Vector CTD criterion applied to mixed mode fatigue crack growth. Fatigue Fract Eng Mater Struct 1989;12(1):59–65. http://dx.doi.org/10.1111/j.1460-2695.1989.tb00508.x.

[17] Ma X, Wang Y, Wang X, Yin W, Liu L, Xu J. Investigation on fatigue crack propagation behaviour of U71Mn and U75V rails using peridynamics. Eng Fract Mech 2023;281:109097. http://dx.doi.org/10.1016/j.engfracmech.2023.109097.

[18] Polančec T, Lesičar T, Tonković Z, Glodež S. Modelling of rolling-contact fatigue pitting phenomena by phase field method. Wear 2023;532–533:205068. http://dx.doi.org/10.1016/j.wear.2023.205068.

[19] CEN. Railway applications - track - rail - Part 1: vignole railway rails 46 kg/m and above. EN 13674-1:2011. European Committee for Standardization; 2011.

[20] ABAQUS/standard user's manual (version 2020). Dassault Systèmes Simulia Corp; 2020.

[21] Belytschko T, Black T. Elastic crack growth in finite elements with minimal remeshing. Internat J Numer Methods Engrg 1999;45:601–20. http://dx.doi.org/10.1002/(SICI)1097-0207(19990620)45:5<601::AID-NME598>3.0.CO;2-S.

[22] Moës N, Dolbow J, Belytschko T. A finite element method for crack growth without remeshing. Internat J Numer Methods Engrg 1999;46:131–50. http://dx.doi.org/10.1002/(SICI)1097-0207(19990910)46:1<131::AID-NME726>3.0.CO;2-J.

[23] Timoshenko SP, J.N Goodier. Theory of elasticity. McGraw-Hill; 1951, 506 p.

[24] Roeleveld T. Measurement of wheel–rail contact forces. In: Symposium of advances in contact mechanics: a tribute to Prof. J.J.Kalker, Delft, The Netherlands. 2008.

[25] Skrypnyk R, Nielsen JCO, Ekh M, Pålsson BA. Metamodelling of wheel–rail normal contact in railway crossings with elasto-plastic material behaviour. Eng Comput 2019;35:139–55. http://dx.doi.org/10.1007/s00366-018-0589-3.

[26] Ekberg A, Åkesson B, Kabo E. Wheel/rail rolling contact fatigue – Probe, predict, prevent. Wear 2014;314(1–2):2–12. http://dx.doi.org/10.1016/j.wear.2013.12.004.

[27] Nielsen JCO, Igeland A. Vertical dynamic interaction between train and track influence of wheel and track imperfections. J Sound Vib 1995;187(5):825–39. http://dx.doi.org/10.1006/jsvi.1995.0566.

[28] Andersson R, Larsson F, Kabo E. Evaluation of stress intensity factors under multiaxial and compressive conditions using low order displacement or stress field fitting. Eng Fract Mech 2018;189:204–20. http://dx.doi.org/10.1016/j.engfracmech.2017.11.015.

[29] Sandström J, Ekberg A. Predicting crack growth and risks of rail breaks due to wheel flat impacts in heavy haul operations. Proc Inst Mech Eng F 2009;223(2):153–61. http://dx.doi.org/10.1243/09544097JRRT224.

[30] Kaneta M, Murakami Y. Propagation of semi-elliptical surface cracks in lubricated rolling/sliding elliptical contacts. J Tribol 1991;113(2):270–5. http://dx.doi.org/10.1115/1.2920616.

[31] Sih GC. Mechanics of fracture initiation and propagation. Springer Netherlands; 1991, 410 p.

[32] Pook LP. The significance of mode 1 branch cracks for combined mode failure. In: Fracture and fatigue, elasto-plasticity, thin sheet and micromechanisms problems. 1980, p. 143–53. http://dx.doi.org/10.1016/B978-0-08-026161-4.50169-2.

[33] Pook LP. The fatigue crack direction and threshold behaviour of mild steel under mixed mode I and III loading. Int J Fatigue 1985;7:21–30. http://dx.doi.org/10.1016/0142-1123(85)90004-0.

[34] Schöllmann M, Richard HA, Kullmer G, Fulland M. A new criterion for the prediction of crack development in multiaxially loaded structures. Int J Fract 2002;117:129–41. http://dx.doi.org/10.1023/A:1020980311611.

[35] Richard HA, Fulland M, Sander M. Theoretical crack path prediction. Fatigue Fract Eng Mater Struct 2005;28(1–2):3–12. http://dx.doi.org/10.1111/j.1460-2695.2004.00855.x.

[36] Floros D, Ekberg A, Larsson F. Evaluation of crack growth direction criteria on mixed-mode fatigue crack growth experiments. Int J Fatigue 2019;129:105075. http://dx.doi.org/10.1016/j.ijfatigue.2019.04.013.

[37] Floros D, Ekberg A, Larsson F. Evaluation of mixed-mode crack growth direction criteria under rolling contact conditions. Wear 2020;448–449:203184. http://dx.doi.org/10.1016/j.wear.2020.203184.

[38] Sun CT, Jin Z-H. Fracture mechanics. Academic Press; 2012, 311 p, http://dx.doi.org/10.1016/C2009-0-63512-1.

[39] Paris P, Erdogan F. A critical analysis of crack propagation laws. J Basic Eng 1963;85(4):528–33. http://dx.doi.org/10.1115/1.3656900.

[40] Wong SL, Bold PE, Brown MW, Allen RJ. Fatigue crack growth rates under sequential mixed-mode I and II loading cycles. Fatigue Fract Eng Mater Struct 2000;23(8):667–74. http://dx.doi.org/10.1046/j.1460-2695.2000.00342.x.

[41] Socie D, Marquis G. Multiaxial fatigue. SAE International; 2000, 484 p.

[42] Skyttebol A, Josefson BL, Ringsberg JW. Fatigue crack growth in a welded rail under the influence of residual stresses. Eng Fract Mech 2005;72:271–85. http://dx.doi.org/10.1016/j.engfracmech.2004.04.009.

[43] MATLAB 9.7.0.1190202 (version R2019b). The MathWorks Inc; 2019.

[44] Stock R, Pippan R. RCF and wear in theory and practice—The influence of rail grade on wear and RCF. Wear 2011;271(1–2):125–33. http://dx.doi.org/10.1016/j.wear.2010.10.015.

[45] Heyder R, Girsch G. Testing of HSH® rails in high-speed tracks to minimise rail damage. Wear 2005;258(7–8):1014–21. http://dx.doi.org/10.1016/j.wear.2004.03.050.

[46] D4.1.4 Rail degradation algorithms, INNOTRACK (project no. TIP5-CT-2006-031415O) report. 2009, 41 p.

[47] Ekberg A, Kabo E. Surface fatigue initiated transverse defects and broken rails – an International Review. 2014, 24 p.